#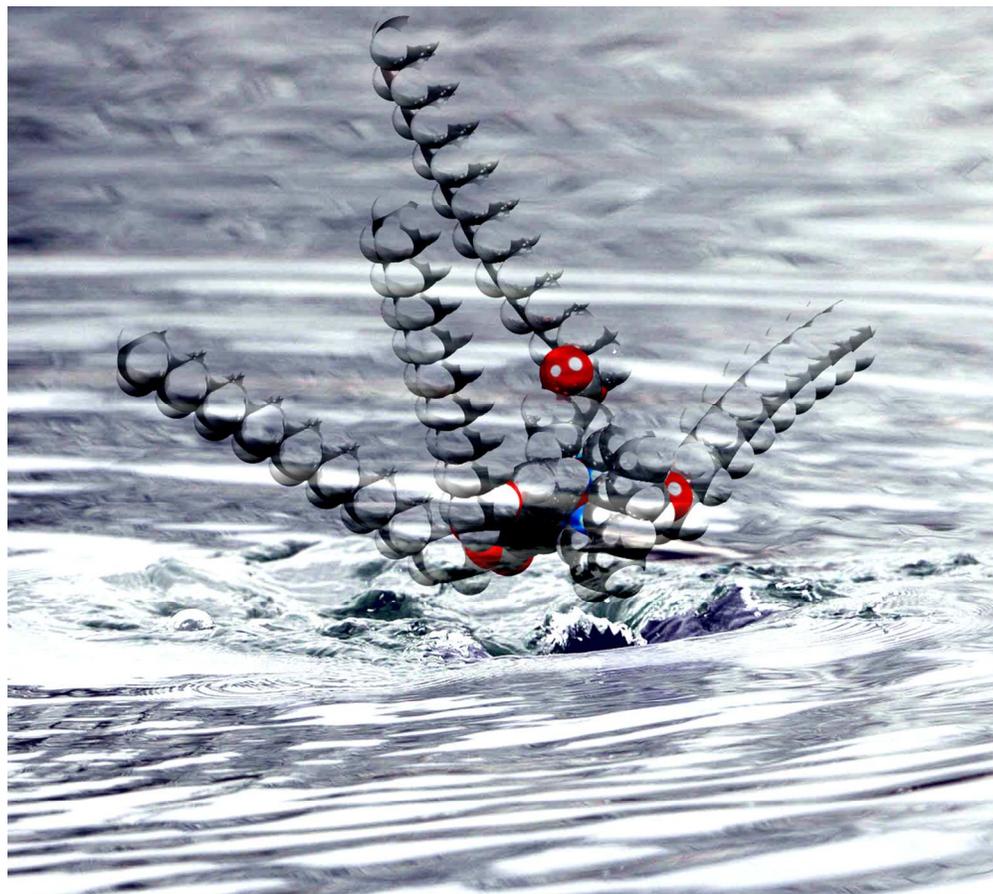 Assembling model tris(bipyridine)ruthenium(II) photosensitizers into ordered monolayers in the presence of the polyoxometallate anion [Co4(H2O)2(α-PW9O34)2]10–

SCHOLARONE™
Manuscripts

136x122mm (300 x 300 DPI)

TOC

Assembling model tris(bipyridine)ruthenium(II) photosensitizers into ordered monolayers in the presence of a POM water oxidation catalyst

N. S. Murray, J. A. Rudd, A.-C. Chamayou, E. C. Constable, C. E. Housecroft, M. Neuburger and J. A. Zampese

Model ruthenium(II) photosensitizers with peripheral long alkyl chains have been assembled into ordered monolayers on water in the presence or absence of an anionic polyoxometallate. LB films formed on mica substrates are visualized using AFM.

RSC Advances

RSC**Publishing**

ARTICLE

Assembling model tris(bipyridine)ruthenium(II) photosensitizers into ordered monolayers in the presence of the polyoxometallate anion [Co₄(H₂O)₂(α-PW₉O₃₄)₂]¹⁰⁻

Niamh S. Murray,[a] Jennifer A. Rudd,[a] Anne-Christine Chamayou,[a] Edwin C. Constable,*[a] Catherine E. Housecroft,*[a] Markus Neuburger,[a] and Jennifer A. Zampese[a]

The complexes cis-[Ru($\mathbf{1}$)$_2$Cl$_2$] and [Ru($\mathbf{1}$)$_2$(bpy)][PF$_6$]$_2$ in which $\mathbf{1}$ is dioctadecyl (2,2'-bipyridine)-4,4'-dicarboxylate have been synthesized and fully characterized; the single crystal structures of the *syn,syn*- and *anti,anti*-conformers of $\mathbf{1}$ have been determined. Pressure–area isotherms for monolayers of cis-[Ru($\mathbf{1}$)$_2$Cl$_2$] on water, aqueous Co$_4$POM (Co$_4$POM = K$_{10}$[Co$_4$(H$_2$O)$_2$(α-PW$_9$O$_{34}$)$_2$]) or aqueous KCl subphases exhibit collapse pressures of 25–27 mN/m and mean molecular areas of 220±10 Å^2. The similarities between these isotherms confirm that there are no significant interactions between neutral cis-[Ru($\mathbf{1}$)$_2$Cl$_2$] and the anionic Co$_4$POM cluster as the monolayer is formed. In contrast, use of the cationic [Ru($\mathbf{1}$)$_2$(bpy)]$^{2+}$ complex results in higher collapse pressures on pure water (54 mN/m) or aqueous KPF$_6$ (48 mN/m) subphases, but a collapse pressure of only 17 mN/m on an aqueous Co$_4$POM subphase. The data are consistent with the monolayer forming at the air–Co$_4$POM interface being significantly less stable than that at the air–water interface, and point to substantial electrostatic interactions between [Ru($\mathbf{1}$)$_2$(bpy)]$^{2+}$ and the anionic Co$_4$POM which can lead to a reduction in the integrity of the film. The introduction of DODA (DODA = dimethyldioctyldecylammonium bromide) stabilizes the monolayers on aqueous Co$_4$POM; mole ratios of [Ru($\mathbf{1}$)$_2$(bpy)][PF$_6$]$_2$: DODA of 1 : 5 and 1 : 20 lead to collapse pressures of 41 and 53 nM/m, respectively. Brewster angle microscopy has been used to image the monolayers and to monitor the effects of the presence of DODA. Langmuir-Blodgett (LB) films of cis-[Ru($\mathbf{1}$)$_2$Cl$_2$] and [Ru($\mathbf{1}$)$_2$(bpy)][PF$_6$]$_2$ with and without Co$_4$POM have been produced on mica substrates. Atomic force microscopy reveals that LB films formed in a single dipping cycle of cis-[Ru($\mathbf{1}$)$_2$Cl$_2$] from a water subphase are distinct from those formed on aqueous Co$_4$POM. The former consists of islands of height ≈ 3, 6 or 9 nm; these values compare with a modelled molecular diameter of cis-[Ru($\mathbf{1}$)$_2$Cl$_2$] of ≈3 nm and are consistent with the formation of mono-, bi-, or trilayers of cis-[Ru($\mathbf{1}$)$_2$Cl$_2$]. In contrast, LB films formed from cis-[Ru($\mathbf{1}$)$_2$Cl$_2$] on aqueous Co$_4$POM consist of small aggregates of variable height. LB films formed from [Ru($\mathbf{1}$)$_2$(bpy)][PF$_6$]$_2$ on aqueous subphase exhibit small aggregates but there is a very low surface coverage of the complex on mica (2 domains/μ□^{2}); the coverage increases (18 domains/μ□^{2}) when the films are formed in the presence of Co$_4$POM but is significantly lower than for cis-[Ru($\mathbf{1}$)$_2$Cl$_2$] (75 domains/μ□^{2}). No significant difference in the morphology of the LB films containing [Ru($\mathbf{1}$)$_2$(bpy)][PF$_6$]$_2$ is observed in the presence of DODA.

Introduction

Water splitting, the conversion of liquid water to dihydrogen and dioxygen by means of visible light energy, is one of the Holy Grails of modern materials chemistry.[1] Particular interest has centred upon photoelectrochemical[2] and photocatalytic[3]

water splitting systems. Much inspiration has derived from our increasing knowledge of the biological machines which are involved in photosynthesis, and increasingly detailed understanding of photosystem I and photosystem II has led to the realization that complex interacting molecular machinery

needs to be organised in a precise spatial and temporal manner to efficiently transfer electrons and holes to their metabolic end-destinations.[4] Both photosystem I and photosystem II include some 100 or more components all precisely arranged to optimize electron or energy transfer. Supramolecular chemistry was conceived of as "chemistry beyond the molecule" and developed in the hope of understanding in detail the intermolecular interactions that will allow the precise and exquisite arrangement of molecular components in synthetic functional machines.[5] To date, this challenge has not been fully realised.

Although biological processes occur in aqueous media, they do not usually occur in aqueous solution, and the organization of molecular components in biology is not one of orienting multiple species in solution, but rather within a highly organized manifold, the phospholipid membrane. The crucial recognition that many of the most critical biological transformations occur at the interface between the membrane and aqueous medium has been crucial in developing new functional synthetic machines.[6] For synthetic approaches, the membrane-aqueous interface can be usefully replaced by the solid-aqueous interface and the choice of solid substrates may be used to optimize the arrangement of molecular components in two dimensions, to specifically tailor the chemistry by which the components are anchored to the surface, and to allow the selective addressing of components through light, electrical or other means. This technique was pioneered by Whitten,[7] Gaines[8] and coworkers who used surfactant tris(bipyridine) ruthenium(II) complexes on a solid glass substrate as water oxidation catalysts. Since then, many types of ruthenium-based water oxidation catalysts have been reported and reviewed.[9] An emerging class of compounds for water oxidation catalysis are the polyoxometallates (POMs),[10] most notably the all inorganic cobalt-containing POM reported by the Hill group in 2010,[11] which in conjunction with a ruthenium-bipyridine photosensitizer was found to be an effective water oxidation catalyst. More recently, the Hill group has investigated the possibility of water oxidation catalysis at a solid-aqueous interface where the ruthenium sensitizer is immobilized on a metal oxide surface and the POM is in aqueous solution.[12]

In this paper we present a novel way of examining this system via the use of Langmuir-Blodgett (LB) films. This technique allows for transfer of ordered monolayers of both POM and the bis- or tris(bipyridine) ruthenium(II) photosensitizer onto a conducting substrate for use in a water splitting device. Mica was chosen as a test substrate because it is easy to cleave into atomically flat regions and has a negatively charged surface appropriate for the electrostatic binding of a cationic ruthenium(II) complex.

Experimental

General

Microwave reactions were carried out in a Biotage Initiator 8 reactor. Bruker Avance III-400 or Avance III-500 NMR spectrometers were used to record ^{1}H and ^{13}C NMR spectra; chemical shifts were referenced to residual solvent peaks (TMS = δ 0 ppm). Infrared spectra of solid samples were recorded using a Shimadzu 8400S instrument with Golden Gate accessory; those of the LB film samples were recorded on a Perkin Elmer FT-IR Spectrum Two spectrophotometer. Electrospray ionization (ESI) and MALDI-TOF mass spectra were recorded using Bruker esquire 3000plus and Bruker microflex spectrometers, respectively. Absorption and emission spectra were recorded with an Agilent 8453 spectrophotometer and Shimadzu RF-5301 PC spectrofluorometer, respectively. Quantum yields were determined using an absolute PL quantum yield spectrometer C11347 Quantaurus_QY (Hamamatsu), and lifetimes with a Compact Fluorescence lifetime Spectrometer C11367 Quantaurus-Tau (Hamamatsu).

Atomic force microscopy (AFM) data was obtained using a Bruker Dimension 3100 Multimode atomic force microscope (Bruker, Santa Barbara, CA) working in air, using silicon cantilevers with an Al reflective layer on the detector side, in tapping mode (Nanosensors pointprobe-plus).

Isotherms were obtained using a KSV Inc. (Finland) Langmuir-Blodgett Teflon® trough (area 420 cm^2) with a Brewster angle microscope (BAM) setup (EP^{3}SW system, Accurion, Göttingen, Germany). LB films were formed on a KSV Inc. (Finland) Langmuir-Blodgett Teflon® trough (area 242 cm^2) equipped with a Wilhelmy plate. All measurements were made at 22 °C using bidistilled water (pH 7.0).

2,2'-Bipyridine-4,4'-dicarboxylic acid was purchased from Fluorochem and used as received. K$_{10}$[Co$_4$(H$_2$O)$_2$(α-PW$_9$O$_{34}$)$_2$][11] (abbreviated to Co$_4$POM) and [Ru(COD)Cl$_2$][13] were prepared according to literature procedures. Dimethyldioctyldecylammonium bromide (DODA) was purchased from Sigma Aldrich and used as received.

Compound 1

Compound **1** was prepared using modifications of literature procedures.[14] Toluene[15] was used as solvent during treatment of 2,2'-bipyridine-4,4'-dicarboxylic acid (0.40 g, 1.64 mmol) with thionyl chloride (15 mL) and subsequent esterification using octadecanol (1.06 g, 3.92 mmol). Compound **1** was recrystallized from CHCl$_3$/EtOH (1.12 g, 1.49 mmol, 90.9%). ^{1}H NMR (400 MHz, CDCl$_3$) δ / ppm 8.96 (ddd, J = 8.7, 1.6, 0.9 Hz, 2H, H^6), 8.87 (ddd, J = 5.0, 1.9, 0.9 Hz, 2H, H^3), 7.90 (m, 2H, H^5), 4.39 (t, J = 6.8 Hz, 4H, H^{OCH_2}), 1.81 (m, 4H, H^{OCH_2CH_2}), 1.44 (m, 4H, H^{OCH_2CH_2CH_2}), 1.40-1.19 (m, 56H, overlapping H^{CH_2}), 0.87 (t, J = 6.7 Hz, 6H, H^{Me}).

cis-[Ru(1)$_2$Cl$_2$]

Compound **1** (300 mg, 0.401 mmol) and [Ru(COD)Cl$_2$] (56.4 mg, 0.202 mmol) were dissolved in DMF (4 mL). The mixture was heated at 100 °C in a microwave reactor for 1 h. Solvent was removed *in vacuo* from the resulting black mixture and the product was purified by column chromatography (SiO$_2$, CH$_2$Cl$_2$ with 5% MeOH). The second band was collected yielding black cis-[Ru(**1**)$_2$Cl$_2$] (160 mg, 0.096 mmol, 47.5%). ^{1}H NMR (500 MHz, CDCl$_3$) δ / ppm 10.44 (d, J = 5.9 Hz, 2H, H^{A6}), 8.83 (d, J

= 1.8 Hz, 2H, H^{A3}), 8.65 (d, J = 1.7 Hz, 2H, H^{B3}), 8.15 (dd, J = 5.9, 1.7 Hz, 2H, H^{A5}), 7.71 (d, J = 6.0 Hz, 2H, H^{B6}), 7.49 (dd, J = 5.9, 1.7 Hz, 2H, H^{B5}), 4.49 (t, J = 6.8 Hz, 4H, $H^{OCH_2 \text{ ring A}}$), 4.34 (t, J = 6.8 Hz, 4H, $H^{OCH_2 \text{ ring B}}$), 1.87 (m, 4H, $H^{OCH_2CH_2 \text{ ring A}}$), 1.73 (m, 4H, $H^{OCH_2CH_2 \text{ ring B}}$), 1.48-1.19 (m, 120H, overlapping H^{CH_2}), 0.87 (t, J = 6.9 Hz, 12H, H^{Me}). ^{13}C NMR (126 MHz, CDCl$_3$) δ / ppm 164.4 ($C^{C=O \text{ ring A}}$), 163.6 ($C^{C=O \text{ ring B}}$), 160.4 (C^{B2}), 158.0 (C^{A2}), 155.2 (C^{A6}), 152.5 (C^{B6}), 136.3 (C^{A4}), 135.0 (C^{B4}), 125.0 (C^{A5}), 124.5 (C^{B5}), 121.8 (C^{B3}), 121.6 (C^{A3}), 66.9 ($C^{OCH_2 \text{ ring A}}$), 66.4 ($C^{OCH_2 \text{ ring B}}$), 31.9 ($C^{CH_2CH_2Me}$), 29.5 (overlapping C^{CH_2}), 29.3 ($C^{OCH_2CH_2CH_2CH_2 \text{ ring A}}$), 29.1 ($C^{OCH_2CH_2CH_2CH_2 \text{ ring B}}$), 28.6 ($C^{OCH_2CH_2 \text{ ring A}}$), 28.5 ($C^{OCH_2CH_2 \text{ ring B}}$), 26.0 ($C^{OCH_2CH_2CH_2 \text{ ring A}}$), 25.8 ($C^{OCH_2CH_2CH_2 \text{ ring B}}$), 22.6 ($C^{CH_2CH_2Me}$), 14.3 ($C^{Me}$). IR (solid, cm^{-1}) 3046 (vw), 3022 (vw), 2918 (s), 2850 (s), 1730 (s), 1711 (m), 1602 (w), 1547 (w), 1465 (m), 1433 (w), 1406 (w), 1317 (m), 1295 (m), 1253 (s), 1233 (s), 1140 (w), 1124 (m), 1105 (m), 1014 (m), 958 (w), 898 (w), 866 (w), 765 (s), 719 (m), 663 (w) UV-vis (CH$_2$Cl$_2$, 5 × 10^{-5} mol dm^{-3}) λ_{max}/nm (ε × 10^{-3}/dm^3 mol^{-1} cm^{-1}) 308 sh (27.5), 319 (38.8), 427 (13.1), 583 (13.6). MALDI-TOF MS: 1671.4 [M]$^+$ (calc. 1670.1), 1636.3 [M − Cl]$^+$ (calc. 1635.1). Found C 68.07, H 9.33, N 3.48; C$_{96}$H$_{160}$Cl$_2$N$_4$O$_8$Ru·CH$_3$OH requires C 68.44, H 9.71, N 3.29.

[Ru(1)$_2$(bpy)][PF$_6$]$_2$

cis-[Ru(**1**)$_2$Cl$_2$] (100 mg, 0.060 mmoles), 2,2'-bipyridine (11 mg, 0.071 mmoles) and AgNO$_3$ (20 mg, 0.12 mmoles) were heated at reflux in EtOH (6 mL) for 30 min. After the solution had cooled to room temperature, CH$_2$Cl$_2$ (20 mL) was added and the solution was transferred to a separating funnel with a saturated aqueous NH$_4$PF$_6$ (20 mL). The organic layer was collected and the aqueous layer washed with CHCl$_2$ (20 mL). The washings were combined and solvent removed *in vacuo* to yield a red solid. This was purified by column chromatography (SiO$_2$, CH$_2$Cl$_2$ with 5% MeOH). The third band was collected and [Ru(**1**)$_2$(bpy)][PF$_6$]$_2$ was isolated as a red solid (60 mg, 0.029 mmol, 48%). ^{1}H NMR (500 MHz, CDCl$_3$) δ/ppm 8.88 (m, 4H, H^{A3+B3}), 8.36 (d, J = 8.2 Hz, 2H, H^{C3}), 8.02 (m, 6H, $H^{C4+A5/B5+A6/B6}$), 7.97 (m, 4H, $H^{A5/B5+A6/B6}$), 7.74 (dd, J = 5.7, 1.4 Hz, 2H, H^{C6}), 7.50 (ddd, J = 7.2, 5.7, 1.3 Hz, 2H, H^{C5}), 4.38 (m, 8H, $H^{OCH_2 \text{ rings A+B}}$), 1.77 (m, 8H, $H^{OCH_2CH_2 \text{ rings A+B}}$), 1.39 (m, 8H, $H^{OCH_2CH_2CH_2 \text{ rings A+B}}$), 1.25 (m, 112H, overlapping H^{CH_2}), 0.87 (t, J = 6.9 Hz, 12H, H^{Me}). ^{13}C NMR (126 MHz, CDCl$_3$) δ / ppm 163.2 ($C^{C=O \text{ rings A+B}}$), 156.9 ($C^{A2/B2}$), 156.4 ($C^{A2/B2}$), 155.9 ($C^{C2}$), 153.4 ($C^{A6/B6}$), 153.1 ($C^{A6/B6}$), 151.9 ($C^{C6}$), 139.6 ($C^{A4+B4}$), 138.8 ($C^{C4}$), 128.8 ($C^{C5}$), 127.9 ($C^{A5/B5}$), 127.7 ($C^{A5/B5}$), 124.1 ($C^{C3}$), 123.0 ($C^{A3+B3}$), 67.1 ($C^{OCH_2}$), 32.1 ($C^{CH_2CH_2Me}$), 29.9 (overlapping C^{CH_2}), 29.8 (C^{CH_2}), 29.7 (C^{CH_2}), 29.5 (C^{CH_2}), 29.4 ($C^{OCH_2CH_2CH_2CH_2}$), 28.4 ($C^{OCH_2CH_2}$), 26.0 ($C^{OCH_2CH_2CH_2}$), 22.8 ($C^{CH_2CH_2Me}$), 14.3 (C^{Me}). IR (solid/cm^{-1}) 3108 (w), 3082 (w), 2918 (s), 2850 (m), 1727 (m), 1605 (w), 1554 (w), 1467 (m), 1410 (m), 1320 (m), 1247 (s), 1126 (m), 1022 (w), 954 (w), 873 (w), 834 (s), 767 (s), 720 (m), 663 (w), 557 (s). UV-vis (CH$_2$Cl$_2$, 5 × 10^{-5} mol dm^{-3}) λ_{max}/nm (ε × 10^{-3}/dm^3 mol^{-1} cm^{-1}) 292 sh (37.8), 308 (50.3), 354 (11.3), 395 (7.6), 434 (12.5), 473 (15.4). ESI-MS: 877.7 [M − 2PF$_6$]$^{2+}$

(calc. 877.6). Found C 62.31, H 8.47, N 4.13; C$_{106}$H$_{168}$F$_{12}$N$_6$O$_8$P$_2$Ru requires C 62.24, H 8.28, N 4.11.

Crystallography

Data were collected on a Bruker Kappa APEX2 diffractometer with data reduction, solution and refinement using the programs APEX2[16] and either SIR92[17] and CRYSTALS,[18] or SHELXL97.[19] ORTEP-type diagrams and structure analysis used Mercury v. 3.0.[20,21]

Compound 1: conformer I

C$_{48}$H$_{80}$N$_2$O$_4$, M = 749.14, colourless plate, triclinic, space group P–1, a = 5.3390(11), b = 7.4715(16), c = 28.443(6) Å, α = 85.669(15), β = 89.406(16), γ = 76.688(15)^o, U = 1100.9(4) Å^3, Z = 1, D_c = 1.130 Mg m^{-3}, μ(Cu-Kα) = 0.539 mm^{-1}, T = 123 K. Total 11259 reflections, 3750 unique, R_{int} = 0.0766. Refinement of 2223 reflections (245 parameters) with I >2σ (I) converged at final R1 = 0.0740 (R1 all data = 0.1626), wR2 = 0.2239 (wR2 all data = 0.2562), gof = 1.051. CCDC 977631.

### Compound 1: conformer II

C$_{48}$H$_{80}$N$_2$O$_4$, M = 749.17, colourless block, triclinic, space group P–1, a = 4.9987(11), b = 5.3505(10), c = 41.561(8) Å, α = 92.041(7), β = 92.798(7), γ = 90.983(7)^o, U = 1109.3(4) Å^3, Z = 1, D_c = 1.121 Mg m^{-3}, μ(Mo-Kα) = 0.070 mm^{-1}, T = 123 K. Total 9800 reflections, 5357 unique, R_{int} = 0.049. Refinement of 2456 reflections (244 parameters) with I >2σ (I) converged at final R1 = 0.1325 (R1 all data = 0.1856), wR2 = 0.0982 (wR2 all data = 0.1300), gof = 0.9591. CCDC 977632.

Preparation of Langmuir monolayers and Langmuir-Blodgett films

cis-[Ru(**1**)$_2$Cl$_2$], [Ru(**1**)$_2$(bpy)][PF$_6$]$_2$ or [Ru(**1**)$_2$(bpy)][PF$_6$]$_2$: DODA mixtures with 1 : 0.5, 1 : 5, and 1 : 20 molar ratios dissolved in CHCl$_3$ were used as spreading solutions. A volume (20 to 40 µ□) of these solutions was dropped carefully onto the aqueous subphase and the solvent was allowed to evaporate for 10 min prior to the start of compression experiments. To obtain pressure–area (π–A) isotherms, the films were compressed until the maximum distance was reached by the barriers. All π–A isotherms are fully reproducible. For transfer onto solid substrates, the films were compressed until they reached the 'solid' phase of the isotherm, i.e. 22 mN/m for transfer of *cis*-[Ru(**1**)$_2$Cl$_2$] on water, 22 mN/m *cis*-[Ru(**1**)$_2$Cl$_2$] on Co$_4$POM (2.7 × 10^{-7} M, 27 mg / 2L), 48 mN/m [Ru(**1**)$_2$(bpy)][PF$_6$]$_2$ on water, 12 mN/m [Ru(**1**)$_2$(bpy)][PF$_6$]$_2$ on Co$_4$POM, 15 mN/m [Ru(**1**)$_2$(bpy)][PF$_6$]$_2$: DODA 1 : 0.5 mixture on Co$_4$POM, 35 mN/m [Ru(**1**)$_2$(bpy)][PF$_6$]$_2$: DODA 1 : 5 mixture on Co$_4$POM, and 35mN/m [Ru(**1**)$_2$(bpy)][PF$_6$]$_2$: DODA 1:20 mixture on Co$_4$POM. Multilayer films were assembled on the substrates by vertical lifting, i.e. withdrawal and immersion of the substrate through the film. The substrate was allowed to dry in air after each withdrawal for 5 min prior to the next immersion/withdrawal cycle. Unless otherwise stated, the dipping speed was 0.2 cm min^{-1}. Initial experiments were performed on mica substrates (Science Services, V1 Quality

0.15-0.21 mm thickness). The mica sheets were cut to the required size (1 cm × 1.5 cm) and then freshly cleaved before immersion in the subphase.
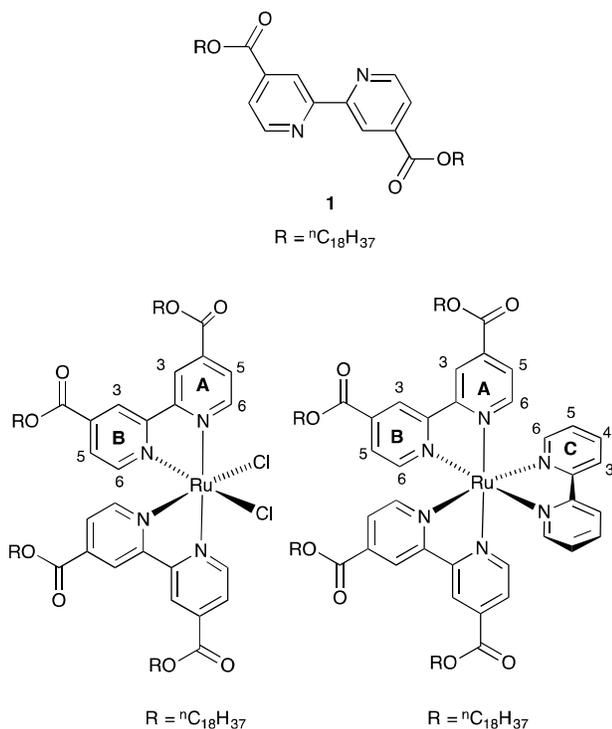
Scheme 1. Ligand and complex structures with labelling scheme for NMR spectroscopic assignments.

(a)

(b)

Fig. 1 ORTEP representations of the structures of **1** (a) *syn,syn*-conformer (symmetry code i = 2−*x*, 2−*y*, 1−*z*) and (b) *anti,anti*-conformer (symmetry code i = −2−*x*, −*y*, 1−*z*). Hydrogen atoms are omitted; ellipsoids are plotted at 50% probability level.

(a)

(b)

Fig. 2. Packing of molecules of **1** in (a) the s-*syn*,s-*syn*-conformer and (b) the s-*anti*,s-*anti*-conformer.

Results and discussion

Structure of compound 1

Compound **1** (Scheme 1) was prepared by esterification of 2,2'-bipyridine-4,4'-dicarboxylic acid using conditions based on those reported by Whitten and coworkers.[14] The assigned ^{1}H NMR spectrum of a CDCl$_3$ solution of **1** (Fig. S1†) is given in the experimental section. Single crystals of two conformers of **1** were grown from MeOH and CHCl$_3$/EtOH, respectively. Both crystallize in the triclinic space group *P*–1 with centrosymmetric molecules (Fig. 1) bearing alkyl chains in extended conformations. The structural determinations confirm the presence of the ester functionality linking the octadecyl chain to the bpy domain, and a symmetrical substitution pattern. Bond parameters are unexceptional. The carbonyl unit of the ester group may adopt a *syn* or *anti* conformation with respect to the 2-substituted pyridine ring to which it is bonded. Figs. 1a and 1b show the *syn,syn*- and *anti,anti*-conformers, respectively. Fig. 2 illustrates that the packing in both conformers is dominated by van der Waals interactions between the alkyl chains; there are no significant face-to-face π-stacking interactions between adjacent bpy domains.
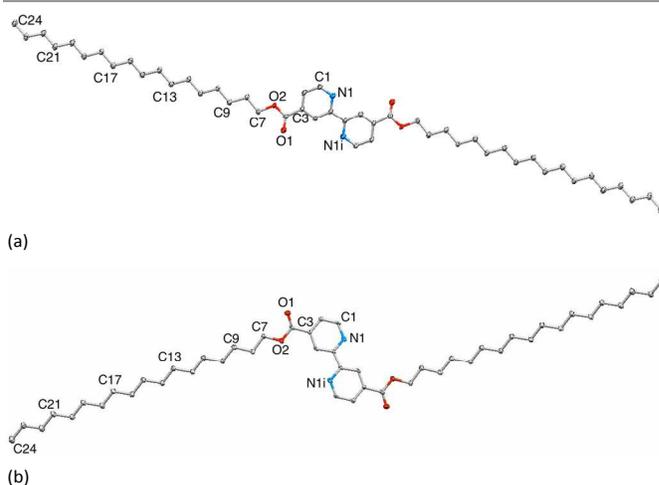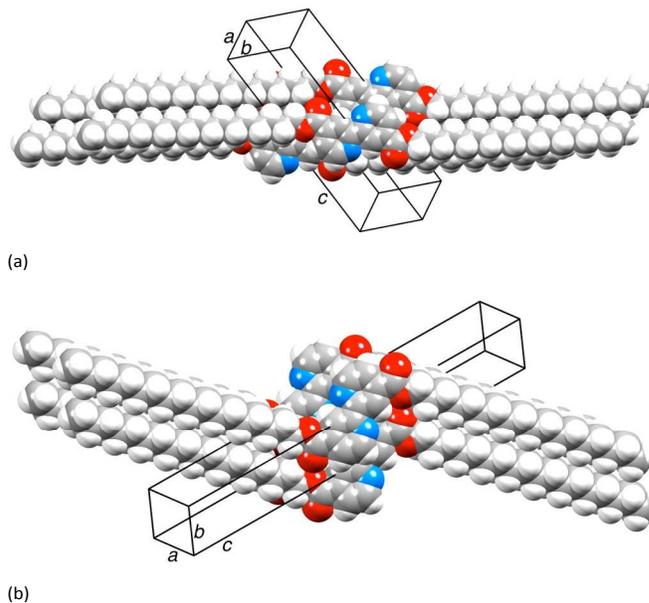
Synthesis and characterization of *cis*-[Ru(1)$_2$Cl$_2$] and [Ru(1)$_2$(bpy)][PF$_6$]$_2$

The most effective route to *cis*-[Ru(**1**)$_2$Cl$_2$] was found to be the reaction of **1** with [Ru(COD)Cl$_2$] under microwave conditions, a methodology used for the preparation of *cis*-[Ru(dcmb)$_2$Cl$_2$] (dcmb = 4,4'-dimethoxycarbonyl-2,2'-bipyridine).[22] After work-up, *cis*-[Ru(**1**)$_2$Cl$_2$] was isolated as a black solid in 47.5% yield. The MALDI-TOF mass spectrum exhibited peak envelopes assigned to [M]$^+$ (*m/z* 1671.4) and [M − Cl]$^+$ (*m/z* 1636.1). The ^{1}H and ^{13}C NMR spectra were consistent with the presence of two pyridine environments and thus confirmed the formation of

the *cis*-isomer of [Ru(**1**)$_2$Cl$_2$] (Scheme 1). The spectra were assigned using standard 2D techniques. Proton H^{A6} (Scheme 1) points towards a chlorido ligand causing its ^{1}H NMR resonance to be shifted to δ̃ 1□□ ppm,[23] in contrast to a signal for H^{B6} which appears at δ 7.71 ppm. This distinction allows the spin systems for the bpy A and B rings to be unambiguously distinguished. Assignment of the ^{13}C NMR signals then follows from the HMQC and HMBC spectra. Magnetic inequivalence in the octyldecyl ester chains attached to the bpy A and B rings is experienced only for the first four CH$_2$ groups (counting from the OCH$_2$ group, see experimental section).

Treatment of *cis*-[Ru(**1**)$_2$Cl$_2$] with a slight excess of bpy in the presence of AgNO$_3$ followed by anion exchange led to the formation of [Ru(**1**)$_2$(bpy)][PF$_6$]$_2$. After purification, the complex was isolated in 48% yield. The base peak in the electrospray mass spectrum at *m/z* 877.7 was consistent with the [M − 2PF$_6$]$^{2+}$ ion, the isotope distribution matching the simulated pattern. Although the two pyridine rings in coordinated ligand **1** are inequivalent (Scheme 1), this is less distinct than in *cis*-[Ru(**1**)$_2$Cl$_2$] and most of the signals for corresponding pairs of ring A/ring B protons overlap in the ^{1}H NMR spectrum. This is also true for pairs of resonances in the ^{13}C NMR spectrum, e.g. one signal at δ 163.2 ppm was assigned to both C$^{C=O}$ nuclei in [Ru(**1**)$_2$(bpy)]$^{2+}$ compared to well separated signals at δ 164.4 and 163.6 ppm for C$^{C=O}$ in rings A and B in *cis*-[Ru(**1**)$_2$Cl$_2$]. It did not prove possible to grow X-ray quality crystals of either ruthenium(II) complex.

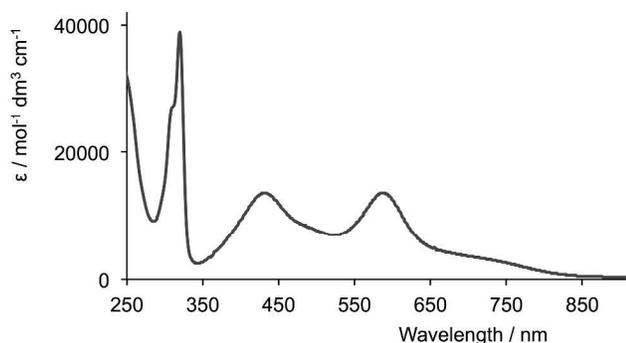**Fig. 3**. Room temperature absorption spectrum of a CH$_2$Cl$_2$ solution of *cis*-[Ru(**1**)$_2$Cl$_2$] (5 x 10^{-5} mol dm^{-3}).

Photophysical properties of *cis*-[Ru(1)$_2$Cl$_2$] and [Ru(1)$_2$(bpy)][PF$_6$]$_2$

Figs. 3 and 4 show the solution absorption and emission spectra of *cis*-[Ru(**1**)$_2$Cl$_2$] and [Ru(**1**)$_2$(bpy)][PF$_6$]$_2$. In the absorption spectrum of *cis*-[Ru(**1**)$_2$Cl$_2$], the intense high energy band arises from π*←π and π*←n transitions. The similarity in the band shape and intensity of the absorption maximum around 310 nm in Figs. 3 and 4 suggests that this band may have the same origins and so is probably dominated by transitions associated with ligand **1** in [Ru(**1**)$_2$(bpy)][PF$_6$]$_2$. The lower intensity band at 350 nm in [Ru(**1**)$_2$(bpy)][PF$_6$]$_2$ may arise from π*←π transitions based on the bpy ligand. The most noticeable difference between the absorption spectra in Figs. 3 and 4 is in

the lower energy bands. The asymmetric band with maxima at 434 and 473 nm in the spectrum of [Ru(**1**)$_2$(bpy)][PF$_6$]$_2$ is reminiscent of the shape of the MLCT band in [Ru(bpy)$_3$]$^{2+}$ [24] but is slightly red-shifted with respect to the latter. The two absorptions at 427 and 583 nm in the spectrum of *cis*-[Ru(**1**)$_2$Cl$_2$] are red-shifted with respect to the corresponding bands at 378 and 554 nm reported for *cis*-[Ru(bpy)$_2$Cl$_2$].[25]

The complex *cis*-[Ru(**1**)$_2$Cl$_2$] is very weakly emissive in CH$_2$Cl$_2$ at room temperature. In contrast, [Ru(**1**)$_2$(bpy)][PF$_6$]$_2$ shows an intense emission at 640 nm (Fig. 4, λ$_{exc}$ = 438 or 482 nm). A quantum yield of 13.5% was determined in solution with a lifetime of 886 ns, and 7% in the solid state (powdered sample) with a lifetime of 823 ns.
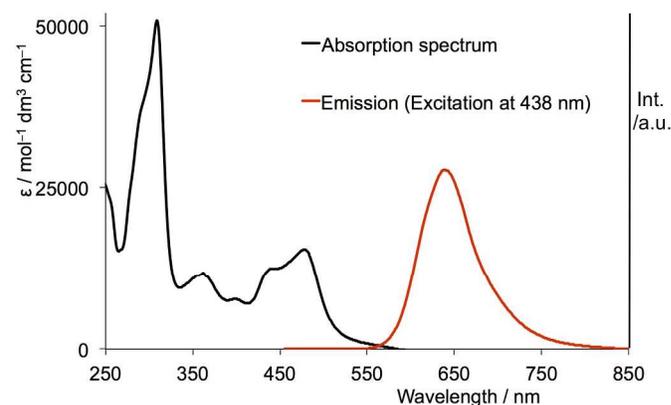

Fig. 4. Room temperature absorption and emission spectra of a CH$_2$Cl$_2$ solution of [Ru(**1**)$_2$(bpy)][PF$_6$]$_2$ (5 x 10^{-5} mol dm^{-3}) in aerated solution.

Preparation of monolayers

The first step towards creating multilayer samples of [Ru(**1**)$_2$(bpy)][PF$_6$]$_2$ and Co$_4$POM was to investigate the monolayer formed by *cis*-[Ru(**1**)$_2$Cl$_2$] on a water subphase. Fig. 5 shows the pressure–area isotherms of *cis*-[Ru(**1**)$_2$Cl$_2$] on a subphase of pure water, Co$_4$POM (2.7 × 10^{-7} M) and aqueous KCl. The films exhibit collapse pressures of between 25 and 27 mN/m, with an estimated mean molecular area of 240 Å^2 for *cis*-[Ru(**1**)$_2$Cl$_2$] on a pure water subphase, 220 Å^2 on an aqueous KCl subphase, and 230 Å^2 on a Co$_4$POM subphase. There is no significant difference between the isotherms of the complex on pure water or on the Co$_4$POM subphase, indicating that there is little or no interaction between the neutral ruthenium complex and the Co$_4$POM as the monolayer is formed. This is, perhaps, not surprising in view of the neutral versus ionic nature of the two species. For verification purposes, a monolayer of *cis*-[Ru(**1**)$_2$Cl$_2$] was formed on an aqueous KCl subphase to confirm the absence of interactions between K$^+$ ions and *cis*-[Ru(**1**)$_2$Cl$_2$]. The similarity between the relevant isotherms shown in Fig. 5 is consistent with there being no interactions. There are only two phase divisions observed in each of these isotherms: that from gaseous to liquid-condensed and liquid-condensed to collapse point. The deviations in the curves observed after the collapse point are

indicative of additional phase transitions. However, for the purposes of our investigation, these were ignored.
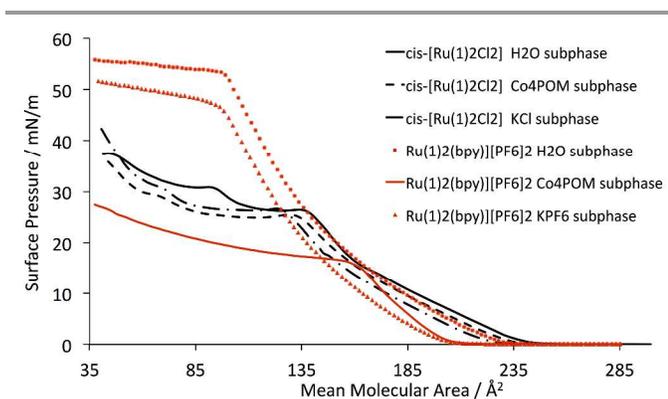

Fig. 5. Isotherms of *cis*-[Ru(**1**)$_2$Cl$_2$], and [Ru(**1**)$_2$(bpy)][PF$_6$]$_2$ on subphases: pure water, Co$_4$POM (2.7 x 10^{-7} M), KCl and KPF$_6$ (2.7 x 10^{-7} M).

The behaviour of Langmuir monolayers formed using [Ru(**1**)$_2$(bpy)][PF$_6$]$_2$ on a pure water subphase showed marked differences from those of the neutral ruthenium complex. Fig. 5 shows that a film formed from [Ru(**1**)$_2$(bpy)][PF$_6$]$_2$ exhibits a significantly higher collapse pressure on both pure water and on KPF$_6$ subphases, implying that these monolayers are more robust than those of *cis*-[Ru(**1**)$_2$Cl$_2$] on either water or aqueous KCl. The collapse pressures for [Ru(**1**)$_2$(bpy)][PF$_6$]$_2$ are 54 mN/m on water and 48 mN/m on aqueous KPF$_6$, compared with 26 mN/m (on water) and 25 mN/m (on aqueous KCl), respectively, for *cis*-[Ru(**1**)$_2$Cl$_2$]. Two phase transitions are observed giving rise to a mean molecular area of 220 Å^2 for [Ru(**1**)$_2$(bpy)][PF$_6$]$_2$ on water in the liquid-condensed phase, and 170 Å^2 for [Ru(**1**)$_2$(bpy)][PF$_6$]$_2$ on water in the solid phase, while the mean molecular areas at the collapse pressures are 165 Å^2 and 195 Å^2 for [Ru(**1**)$_2$(bpy)][PF$_6$]$_2$ on KPF$_6$ subphase in the liquid-condensed and the solid phase, respectively. These values are very similar, implying that there is no significant interaction between the K$^+$ ions in the KPF$_6$ subphase and [Ru(**1**)$_2$(bpy)][PF$_6$]$_2$. However, the isotherm for [Ru(**1**)$_2$(bpy)][PF$_6$]$_2$ on a Co$_4$POM subphase differs considerably. The collapse pressure of 17 mN/m is lower than even *cis*-[Ru(**1**)$_2$Cl$_2$], and only one phase transition occurs, with a mean molecular area of 200 Å^2. This indicates that the monolayer forming at the air–Co$_4$POM interface is much less stable than that at the air–water interface, implying that there is a significant interaction between [Ru(**1**)$_2$(bpy)][PF$_6$]$_2$ and Co$_4$POM.
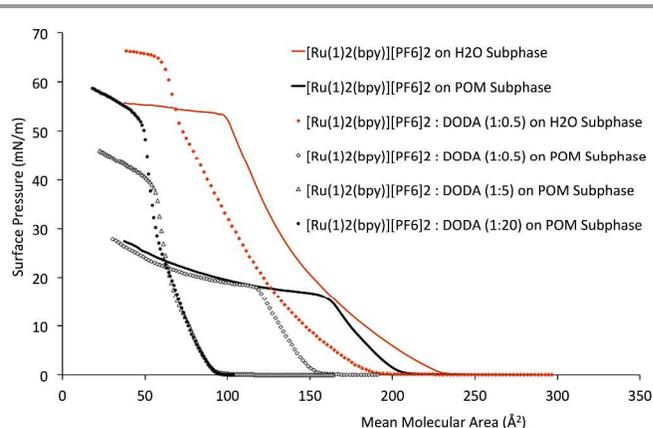

Fig. 6. Isotherms of mixed monolayers of [Ru(**1**)$_2$(bpy)][PF$_6$]$_2$/DODA (1 : 0.5, 1 : 5 and 1 : 20) on pure water and aqueous Co$_4$POM (2.7 x 10^{-7} M) subphases.

Several mixed monolayers of [Ru(**1**)$_2$(bpy)][PF$_6$]$_2$ and DODA on a Co$_4$POM subphase were prepared to establish whether the presence of DODA would stabilize the interactions between [Ru(**1**)$_2$(bpy)][PF$_6$]$_2$ and Co$_4$POM via ionic interactions between the anionic POM in the subphase, and the cationic DODA chains.[26] Three monolayers were prepared in ratios of [Ru(**1**)$_2$(bpy)][PF$_6$]$_2$: DODA of 1 : 0.5, 1 : 5 and 1 : 20 on a Co$_4$POM subphase. Analysis of the resulting isotherms (Fig. 6) reveals that the addition of DODA to the [Ru(**1**)$_2$(bpy)][PF$_6$]$_2$ monolayer has a significant effect on the stability. The collapse pressures of [Ru(**1**)$_2$(bpy)][PF$_6$]$_2$: DODA in a 1 : 0.5 ratio on a Co$_4$POM subphase and [Ru(**1**)$_2$(bpy)][PF$_6$]$_2$ alone on a Co$_4$POM subphase are very similar (18 and 17 mN/m, respectively). However, higher mole fractions of DODA lead to the collapse pressure more than doubling to 41 mN/m and 53 mN/m for [Ru(**1**)$_2$(bpy)][PF$_6$]$_2$: DODA (1 : 5) on Co$_4$POM and [Ru(**1**)$_2$(bpy)][PF$_6$]$_2$/DODA (1 : 20) on Co$_4$POM, respectively. The mean molecular area of the collapse point is also greatly reduced as the ratio of the mole fractions of [Ru(**1**)$_2$(bpy)][PF$_6$]$_2$: DODA changes from 1 : 0 to 1 : 20.

Brewster Angle Microscopy

Brewster angle microscopy (BAM) was used to observe the formation of Langmuir monolayers at the air-water interface during compression of the monolayers, and to visually examine the two-dimensional organization of these monolayers, including the size and shape of the domains and the heterogeneity of the Langmuir-Blodgett films.[27,28] Some examples of the images seen with BAM are shown in Fig. 7. The images of *cis*-[Ru(**1**)$_2$Cl$_2$] and [Ru(**1**)$_2$(bpy)][PF$_6$]$_2$ on a pure water subphase are quite similar at low surface pressures. At the start of the layer compression, the film forms a net-like structure (Fig. 7a and S3a†) with large holes (black areas). The layer compacts very quickly after compression begins, initially forming channels which, with increasing pressure, evolve into a homogenous monolayer (Figs. S2b to d, and S3b to d†). Some pinhole features are observed in the monolayers of both *cis*-[Ru(**1**)$_2$Cl$_2$] and [Ru(**1**)$_2$(bpy)][PF$_6$]$_2$ at ≈2 to 3 mN/m (Fig. S2c

and S3d†). Once the collapse point is reached, fully homogenous layers are observed for both complexes (Fig. S2e and S3e†).
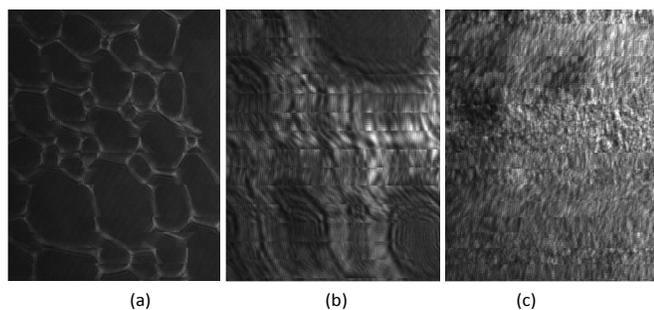

Fig. 7. Brewster angle microscopy images of [Ru(**1**)$_2$(bpy)][PF$_6$]$_2$ on (a) pure water (0.01 mN/m), (b) aqueous KPF$_6$ (0.02 mN/m) and (c) Co$_4$POM (0.06 mN/m) subphases.

Inspection of the BAM images of *cis*-[Ru(**1**)$_2$Cl$_2$] and [Ru(**1**)$_2$(bpy)][PF$_6$]$_2$ on aqueous KCl and KPF$_6$ (Fig. 7b) subphases, respectively, up to pressures of 25 mN/m reveals only small differences between them (Figs. S4a versus S5a†). This is to be expected as we do not anticipate any significant interaction between the complexes and these subphases, consistent with the π–A isotherms being very similar below a pressure of 25 mN/m. Similar net-like structures are observed before compression begins, followed by a monolayer with some pin-hole features (Figs. S4b and S5b†). After the collapse point, very bright domains were observed in the BAM images of the *cis*-[Ru(**1**)$_2$Cl$_2$]-containing Langmuir films, suggesting that a bi- or multi-layer had formed in certain regions (26.90 mN/m, Fig. S4e†). In contrast, this did not occur in the images of Langmuir films formed by [Ru(**1**)$_2$(bpy)][PF$_6$]$_2$ where even at 51.42 mN/m (Fig. S5e†), a uniformly bright phase fully covered the surface, consistent with a homogenous monolayer.

We begin to see a marked difference between the two complexes upon inspection of the BAM images on a Co$_4$POM subphase. The net-like structure observed at the pre-compression phase for *cis*-[Ru(**1**)$_2$Cl$_2$] (Fig. S2a†) and just afterwards is replaced by channels and holes in an already, more uniform layer (Fig. S6a†). However, the corresponding image of the film formed with [Ru(**1**)$_2$(bpy)][PF$_6$]$_2$ shows a layer containing very small holes and channels (Fig. 7c). Once compression begins (Fig. S7b†), the layer very quickly becomes homogeneous and only a few channels remain above a pressure of 1 mN/m for both complexes (Figs. S6c–e and S7c–e†).

The BAM images of the monolayers containing [Ru(**1**)$_2$(bpy)][PF$_6$]$_2$ and DODA (1 : 0.5) on a pure water subphase, show the presence of a net-like structure (Fig. 8a) immediately after compression. This is reminiscent of the net-like structure shown in Fig. 7a. This quickly compresses and small holes and channels appear as seen in Fig. S8b†. At a pressure of 1.71 mN/m, a continuous bright domain is visible (Fig. S8c†), but by the collapse point, small pin-hole features are observed (Fig. S8e†). The similarities observed in the BAM

images for these two systems are consistent with the similarities between the isotherms of these systems (red curves in Fig. 6). The addition of a small amount of DODA reduces the mean molecular area at which the lift-off point occurs (232 Å^2 for [Ru(**1**)$_2$(bpy)][PF$_6$]$_2$ to 197 Å^2 for [Ru(**1**)$_2$(bpy)][PF$_6$]$_2$/DODA with mole fraction ratio of 1 : 0.5.

The addition of DODA (1 : 0.5, 1 : 5 and 1 : 20 complex : DODA mole fractions) to [Ru(**1**)$_2$(bpy)][PF$_6$]$_2$ on a Co$_4$POM subphase results in marked changes in the BAM images. Small domains of the subphase (dark areas) are observed within a bright layer at the pre-compression stage and just as compression begins (Figs. 8b–d). As the pressure is increased, this quickly gives way to a continuous bright domain with pinhole features for all DODA mixtures (Fig. 8e) and these pinholes persist until the monolayers collapse (Figs. S9–11†).
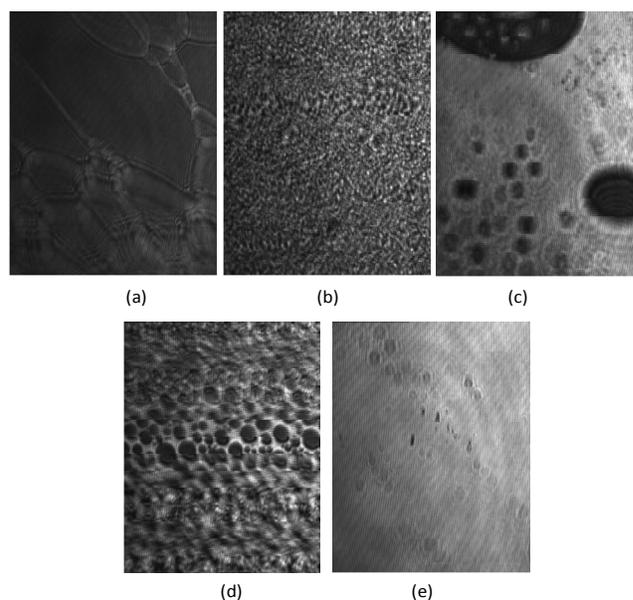

Fig. 8. Brewster angle microscopy images of [Ru(**1**)$_2$(bpy)][PF$_6$]$_2$/DODA (a) 1 : 0.5 on pure water (0.06 mN/m), (b) 1 : 0.5 on Co$_4$POM subphase (0.04 mN/m), (c) 1 : 5 on Co$_4$POM subphase (0.11 mN/m), (d) 1 : 20 on Co$_4$POM subphase (0.05 mN/m), (e) 1 : 0.5 on Co$_4$POM subphase (0.63 mN/m).

**Characterization of LB Films using atomic force microscopy**

Langmuir-Blodgett films of *cis*-[Ru(**1**)$_2$Cl$_2$] and [Ru(**1**)$_2$(bpy)][PF$_6$]$_2$ with and without Co$_4$POM were produced by the vertical dipping method.[29] Films were formed on mica sheets (see experimental section), and the transfer ratio was close to unity for all samples, indicating that Y-type films had been created. Atomic force microscopy (AFM) was used to directly image the surface morphology of the LB films.

Langmuir-Blodgett films were formed by single or multiple dipping cycles. AFM images of LB films of *cis*-[Ru(**1**)$_2$Cl$_2$] on a pure water subphase with one dipping cycle, and on a Co$_4$POM subphase with one, three, and five dipping cycles. The morphology of the film formed by depositing a single layer of *cis*-[Ru(**1**)$_2$Cl$_2$] from a water subphase is significantly different from that formed on a Co$_4$POM subphase. The film from a pure water subphase forms distinct islands (Fig. 9a) with an average

height of 8.8 nm. Fig. 9b shows the line profile corresponding to the line drawn through the image in Fig. 9a, and the two islands included in the profile each has a height of around 3 nm. This corresponds nicely to a diameter of 3 nm for the modelled (using Spartan '08)[30] structure of *cis*-[Ru($\mathbf{1}$)$_2$Cl$_2$] with its alkyl chains extended. While the islands are not uniform in height, they exhibit regions of heights close to 3, 6 or 9 nm. This implies that the islands comprise mono-, bi-, or trilayers of *cis*-[Ru($\mathbf{1}$)$_2$Cl$_2$]. The root mean squared (rms) surface roughness of the sample is 0.59 nm.
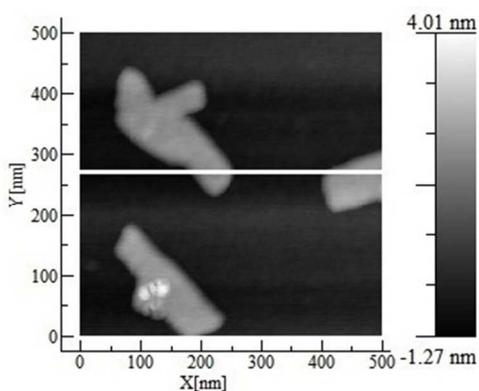

(a)
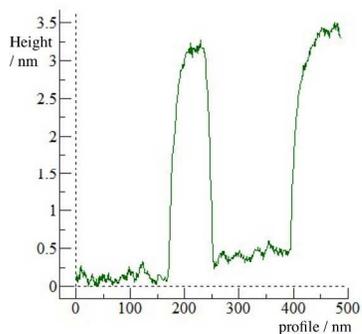
(b)

Fig. 9. (a) AFM height image of *cis*-[Ru($\mathbf{1}$)$_2$Cl$_2$] LB film (one dipping cycle) on mica, transferred from a monolayer formed on pure water subphase. (b) Line profile corresponding to the blue line drawn in (a). The dark area visible between the islands in Fig. 9a is bare mica.

Fig. 10a–c show the LB films formed from monolayers of *cis*-[Ru($\mathbf{1}$)$_2$Cl$_2$] on a Co$_4$POM subphase transferred in one, three, and five dipping cycles. These images indicate that the presence of Co$_4$POM in the subphase induces a significant change in the deposition of the films. The LB film no longer forms islands (the height-dimensions of which correspond to the molecular dimensions of *cis*-[Ru($\mathbf{1}$)$_2$Cl$_2$]) but rather forms small aggregates of variable height. Line profiles are given in Fig. S12†).
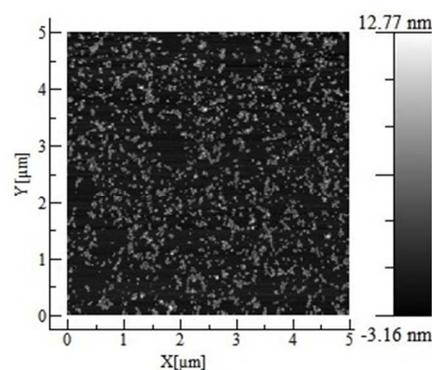
(a)
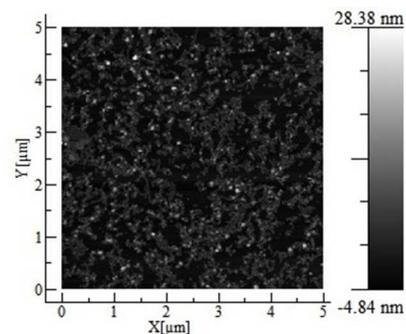
(b)
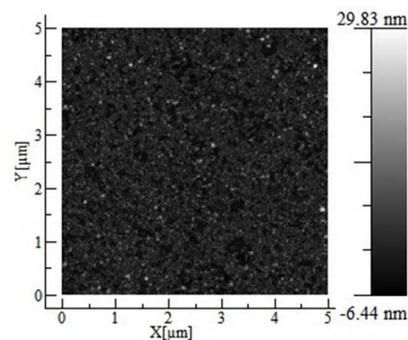
(c)
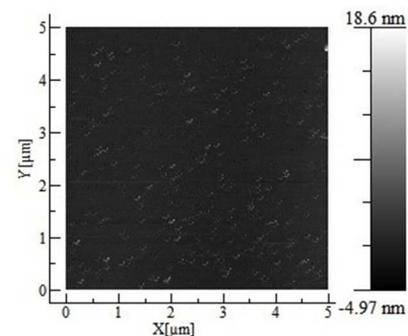
(d)

Fig. 10. AFM height images of (a) *cis*-[Ru($\mathbf{1}$)$_2$Cl$_2$] LB film (one dipping cycle), (b) *cis*-[Ru($\mathbf{1}$)$_2$Cl$_2$] LB film (three dipping cycles), (c) *cis*-[Ru($\mathbf{1}$)$_2$Cl$_2$] LB film (five dipping cycles) and (d) [Ru($\mathbf{1}$)$_2$(bpy)][PF$_6$]$_2$ LB film (five dipping cycles) on mica, transferred from the respective monolayers formed on a Co$_4$POM subphase.

Increasing the number of dipping cycles increases the density of the aggregates on the surface, but does not otherwise significantly impact on the morphology of the LB film. The rms values are 2.17 nm, 3.59 nm, and 3.08 nm for one, three, and five layers, respectively. The slight decrease in the rms from three to five dipping cycles can be attributed to increased loading on the surface. The average height of these aggregates increases from 3.15 nm for one dipping cycle, to 4.84 nm for three and 6.44 nm for five dipping cycles. The formation of aggregates in the *cis*-[Ru(**1**)$_2$Cl$_2$]/Co$_4$POM LB films versus homogeneous monolayers prior to transference to the mica substrate is reminiscent of our observations of the [Ir(ppy)$_2$(ddbpy)][PF$_6$]/EuW$_{10}$ system (ddbpy = 4,4'-bis(3,5-bis(dodecyloxy))benzyloxy-2,2'-bipyridine; EuW$_{10}$ = Na$_9$[Eu(W$_5$O$_{18}$)$_2$]·32H$_2$O.[31]

We now consider the effects of going from *cis*-[Ru(**1**)$_2$Cl$_2$] to [Ru(**1**)$_2$(bpy)][PF$_6$]$_2$, starting with a pure water subphase. There are distinct differences between the transferred LB films of [Ru(**1**)$_2$(bpy)][PF$_6$]$_2$ (Fig. S13†) or *cis*-[Ru(**1**)$_2$Cl$_2$] (Fig. 9a) on a water subphase. Firstly, no islands analogous to those of *cis*-[Ru(**1**)$_2$Cl$_2$] (i.e. islands typically of size 300 - 1000 nm × 50 - 200 nm) on a water subphase are observed. Instead, small aggregates with an average area of approximately 50 nm^2 are apparent. There is very low surface coverage of [Ru(**1**)$_2$(bpy)][PF$_6$]$_2$ on the mica sample. The two samples have the same domain density (2 domains / μm^2), however the rms value (0.18 nm of [Ru(**1**)$_2$(bpy)][PF$_6$]$_2$ vs 0.59 nm of *cis*-[Ru(**1**)$_2$Cl$_2$]) confirms that the surface is mostly bare mica.

Examination of the sample with five dipping cycles of [Ru(**1**)$_2$(bpy)][PF$_6$]$_2$ on a Co$_4$POM subphase (Fig. 10d and Figs. S14a and S14b†) reveals that the surface coverage is greater (18 domains / μm^2 vs 2 domains / μm^2) than on a pure water subphase, but it is significantly lower than the corresponding *cis*-[Ru(**1**)$_2$Cl$_2$] sample (≈ 75 domains / μm^2). No significant difference is observed upon the addition of DODA (Fig. 10d versus Fig. 11, and Figs. S15a and S15b†). The LB film formed by the transfer of a mixed monolayer of [Ru(**1**)$_2$(bpy)][PF$_6$]$_2$/DODA (1 : 20) on a Co$_4$POM subphase gives rise to another sparsely populated sample of small aggregates (see the line profiles in Figs. S15c and S15d†). The density of these aggregates is slightly greater than that of [Ru(**1**)$_2$(bpy)][PF$_6$]$_2$ in the absence of DODA, (42 domains / μm^2, vs. 18 domains / μm^2). Interestingly, the LB film formed by deposition of [Ru(**1**)$_2$(bpy)][PF$_6$]$_2$/DODA (1:5) on POM subphase has a very similar domain density(≈ 41 domains / μm^2), but a slightly greater rms (1.02 nm vs 1.71 nm) and average particle height (2.15 nm vs 3.93 nm) compared with that of [Ru(**1**)$_2$(bpy)][PF$_6$]$_2$/DODA (1:20).
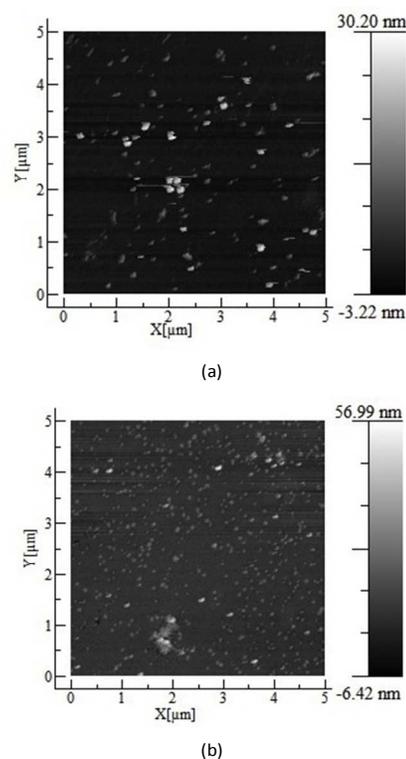

(a)

(b)

Fig. 11. AFM height images of [Ru(**1**)$_2$(bpy)][PF$_6$]$_2$/DODA LB films (five dipping cycles) on mica transferred from monolayers formed on a Co$_4$POM subphase: (a) 1 : 5 and (b) 1 : 20 [Ru(**1**)$_2$(bpy)][PF$_6$]$_2$: DODA mole fraction.

Conclusions

We have described the preparation and characterization of *cis*-[Ru(**1**)$_2$Cl$_2$] and [Ru(**1**)$_2$(bpy)][PF$_6$]$_2$ designed as model photosensitizers which can be assembled into ordered monolayers by virtue of the long alkyl chain substituents. Pressure–area isotherms for monolayers of the *cis*-[Ru(**1**)$_2$Cl$_2$] on water, aqueous Co$_4$POM or aqueous KCl subphases are similar to one another with collapse pressures of 25–27 mN/m and mean molecular areas of 220±10 Å^2. While the presence of Co$_4$POM has no effect on the ordering of the neutral *cis*-[Ru(**1**)$_2$Cl$_2$], a very different scenario is observed for [Ru(**1**)$_2$(bpy)]$^{2+}$. A collapse pressure of 17 mN/m for monolayers of [Ru(**1**)$_2$(bpy)][PF$_6$] on aqueous Co$_4$POM compares with 54 mN/m on water and 48 mN/m on aqueous KPF$_6$ subphases. Thus, the integrity of the cationic monolayer is reduced by the presence of the anionic Co$_4$POM. The monolayer is stabilized by the addition of DODA. LB films of *cis*-[Ru(**1**)$_2$Cl$_2$] and [Ru(**1**)$_2$(bpy)][PF$_6$]$_2$ with and without Co$_4$POM have been formed on mica substrates and the film morphology investigated using AFM. LB films formed in a single dipping cycle of *cis*-[Ru(**1**)$_2$Cl$_2$] from water contain discrete islands, the heights of which are consistent with the presence of mono-, bi-, or trilayers of *cis*-[Ru(**1**)$_2$Cl$_2$]. LB films produced from *cis*-[Ru(**1**)$_2$Cl$_2$] on aqueous Co$_4$POM contain small aggregates of variable height. LB films involving the [Ru(**1**)$_2$(bpy)]$^{2+}$ cation exhibit a very low surface coverage and

there is no significant difference in the presence of DODA. Despite the appearance of homogeneous layers observed by BAM for cis-[Ru($\mathbf{1}$)$_2$Cl$_2$], [Ru($\mathbf{1}$)$_2$(bpy)][PF$_6$]$_2$, [Ru($\mathbf{1}$)$_2$(bpy)][PF$_6$]$_2$/DODA (1 : 5), and [Ru($\mathbf{1}$)$_2$(bpy)][PF$_6$]$_2$/DODA (1 : 20) monolayers, we conclude that all give inhomogeneous films after transfer deposition to mica substrates.

Acknowledgements

Notes and references

[a]Department of Chemistry, University of Basel, Spitalstrasse 51, CH-4056 Basel, Switzerland. Email: edwin.constable@unibas.ch.
† Electronic Supplementary Information (ESI) available: Fig. S1. ^{1}H NMR spectrum of $\mathbf{1}$; Figs. S2–S15: Detailed BAM and AFM images. See DO**I:** 10.1039/b000000x/

1   N. S. Lewis, D. G. Nocera, *Proc. Nat. Acad. Sci.*, 2006, **103**, 15729.

2   A. Fujishima and K. Honda, *Nature*, 1972, **238**, 37; X. Chen, S. Shen, L. Guo and S. S. Mao, *Chem. Rev.*, 2010, **110**, 6503; H. M. Chen, C. K. Chen, R.-S. Liu, L. Zhang, J. Zhang and D. P. Wilkinson, *Chem. Soc. Rev.*, 2012, **41**, 5654; A. Kudo and Y. Miseki, *Chem. Soc. Rev.*, 2009, **38**, 253; Y. Zhao, R. Nakamura, K. Kamiya, S. Nakanishi and K. Hashimoto, *Nature Commun.*, 2013, **4**, 2390.

3   F. E. Osterloh, *Chem. Mater.*, 2007, **20**, 35; N. S. Lewis and D. G. Nocera, *Proc. Nat. Acad. Sci.*, 2006, **103**, 15729; M. Ni, M. K. H. Leung, D. Y. C. Leung and K. Sumathy, *Renew. Sustain. Energy Rev.*, 2007, **11**, 401; J. Nowotny, C. C. Sorrell, T. Bak and L. R. Sheppard, *Solar Energy*, 2005, **78**, 593; R. Abe, *J. Photochem. Photobiol. C*, 2010, **11**, 179.

4   A. W. Rutherford and P. Heathcote, *Photosynthesis Res.*, 1985, **6**, 295; A. W. Rutherford and P. Faller, *Phil. Trans. Royal Soc. B*, 2003, **358**, 245; J. Barber and M. D. Archer, *J. Photochem. Photobiol. A*, 2001, **142**, 97; K. Ferreira, T. Iverson, K. Maghlaoui, J. Barber and S. Iwata, *Science*, 2004, **303**, 1831.

5   *Supramolecular Chemistry: From Molecules to Nanomaterials*, eds. J. W. Steed and P. A. Gale, Wiley, Chichester, 2012; J-M Lehn, *Angew Chem. Int Ed.*, 1998, **27**, 89; J-M Lehn, *Chem. Soc. Rev.*, 2007, **36**, 151.

6   Y. Tachibana, L. Vayssieres and J. R. Durrant, *Nature Photonics*, 2012, **6**, 511; L. Li, L. Duan, Y. Xu, M. Gorlov, A. Hagfeldt and L. Sun, *Chem. Commun.*, 2010, **46**, 7307; M. W. Kanan and D. G. Nocera, *Science*, 2008, **321**, 1072.

7   G. Sprintschnik, H. W. Sprintschnik, P. P. Kirsch and D. G. Whitten, *J. Am. Chem. Soc.*, 1977, **99**, 4947.

8   G. L. Gaines, Jr., P. E. Behnken and S. J. Valenty, *J. Am. Chem. Soc.*, 1978, **100**, 6549.

9   X. Liu and F. Wang, Coord. Chem. Rev., 2012, 256, 1115-1136. H. Yamazaki, A. Shouji, M. Kajita and M. Yagi, *Coord. Chem. Rev.*, 2010, **254**, 2483; F. Puntoriero, A. Sartorel, M. Orlandi, G. La Ganga, S. Serroni, M. Bonchio, F. Scandola and S. Campagna, *Coord. Chem. Rev.*, 2011, **255**, 2594; B. Limburg, E. Bouwman and S. Bonnet, *Coord. Chem. Rev.*, 2012, **256**, 1451.

10 C. Streb, *Dalton Trans.*, 2012, 41, 1651; D.-L. Long, E. Burkholder and L. Cronin, *Chem. Soc. Rev.*, 2007, **36**, 105.

11 Q. Yin, J. M. Tan, C. Besson, Y. V. Geletii, D. G. Musaev, A. E. Kuznetsov, Z. Luo, K. I. Hardcastle and C. L. Hill, *Science*, 2010, **328**, 342.

12 X. Xiang, J. Fielden, W. Rodríguez-Cordoba, Z. Huang, N. Zhang, Z. Luo, D. G. Musaev, T. Lian, and C. L. Hill, *J. Phys. Chem. C*, 2013, **117**, 918.

13 M. O. Albers, T. V. Ashworth, H. E. Oosthuizen, E. Singleton, J. S. Merola and R. T. Kacmarcik, *Inorg. Synth.*, 1989, **26**, 68.

14 G. Sprintschnik, H. W. Sprintschnik, P. P. Kirsch and D. G. Whitten, *J. Am. Chem. Soc.*, 1977, **99**, 4947.

15 T. Ben Hadda, N. Sam, H. Le Bozec and P. H. Dixneuf, *Inorg. Chem. Comm.*, 1999, **2**, 460.

16 Bruker Analytical X-ray Systems, Inc., 2006, APEX2, version 2 User Manual, M86-E01078, Madison, WI.

17 A. Altomare, G. Cascarano, G. Giacovazzo, A. Guagliardi, M. C. Burla, G. Polidori and M. Camalli, *J. Appl. Cryst.*, 1994, **27**, 435.

18 P. W. Betteridge, J. R. Carruthers, R. I. Cooper, K. Prout and D. J. Watkin, *J. Appl. Cryst.*, 2003, **36**, 1487.

19 G. M. Sheldrick, *Acta Crystallogr., Sect. A*, 2008, **64**, 112.

20 I. J. Bruno, J. C. Cole, P. R. Edgington, M. K. Kessler, C. F. Macrae, P. McCabe, J. Pearson and R. Taylor, *Acta Crystallogr., Sect. B* 2002, **58**, 389.

21 C. F. Macrae, I. J. Bruno, J. A. Chisholm, P. R. Edgington, P. McCabe, E. Pidcock, L. Rodriguez-Monge, R. Taylor, J. van de Streek and P. A. Wood, *J. Appl. Cryst.*, 2008, **41**, 466.

22 M. Schwalbe, B. Schäfer, H. Görls, S. Rau, S. Tschierlei, M. Schmitt, J. Popp, G. Vaughan, W. Henry and J. G. Vos, *Eur. J. Inorg. Chem.*, 2008, 3310.

23 See for example: D. Hesek, Y. Inoue, S. R. L. Everitt, H. Ishida, M. Kunieda and M. G. B. Drew, *J. Chem. Soc., Dalton Trans.*, 1999, 3701.

24 A. Juris, V. Balzani, F. Barigelletti, S. Campagna, P. Belser and A. von Zelewsky, *Coord. Chem. Rev.*, 1988, **84**, 85.

25 J. E. Fergusson and G. M. Harris, *J. Chem. Soc. A*, 1966, 1293.

26 See for example: M. Clemente-Leon, C. Mingotaud, C.J. Gomez-Garcia, E. Coronado and P. Delhaes, *Thin Solid Films*, 1998, **327–329**, 439; Y. Iwafuji and C. E. McNamee, *Colloids and Surfaces A*, 2012, **398**, 24; H. Li, J. Zhang and C. Bubeck, *Thin Solid Films*, 2010, **519**, 417.

27 D. Ho☐nig and D. Mo☐bius, *J. Phys. Chem.*, 1991, **95**, 4590.

28 D. Vollhardt, Adv. Colloid Interface Sci., 1996, **64**, 143.

29 M. Sugi, N. Minari, K. Ikegami, S-I. Kuroda, K. Saito, M. Saito, *Thin Solid Films*, 1989, **178**, 157.

30 Spartan '08, v. 1.2.1, Wavefunction Inc., Irvine, CA92612.

31 M. Clemente-León, E. Coronado, A. López-Muñoz, D. Repetto, T. Ito, T. Konya, T. Yamase, E. C. Constable, C. E. Housecroft, K. Doyle and S. Graber, *Langmuir*, 2010, **26**, 1316,